Journal of The Electrochemical Society, **161** (10) H598-H605 (2014)
0013-4651/2014/161(10)/H598/8/$31.00 © The Electrochemical Society

Synthesis of Petal-Like Carbon Nanocapsule@MnO_2 Core-Shell Particles and Their Application in Supercapacitors

Ting-Ting Lee,[a] Jing-Ru Hong,[a] Wei-Chen Lin,[a] Chi-Chang Hu,[b,*] Pu-Wei Wu,[c] and Yuan-Yao Li[a,d,e,z]

[a]*Department of Chemical Engineering, National Chung Cheng University, Chia-Yi 62102, Taiwan*
[b]*Department of Chemical Engineering, National Tsing Hua University, Hsin-Chu 30013, Taiwan*
[c]*Department of Materials Science and Engineering, National Chiao Tung University, Hsin-Chu 300, Taiwan*
[d]*Graduate Institute of Opto-Mechatronics, National Chung Cheng University, Chia-Yi 62102, Taiwan*
[e]*Advanced Institute of Manufacturing with High-Tech Innovations, National Chung Cheng University, Chia-Yi 62102, Taiwan*

Carbon nanocapule (CNC)@MnO_2 core-shell particles are prepared with a reaction of $KMnO_4$ with CNC at 90°C. Birnessite-type MnO_2 nanoflakes are grown on CNC seeds, resulting in CNC@MnO_2 particles with a petal-like structure. The electrochemical characteristics of the prepared materials show that the highest specific capacitance (163 Fg^{-1}) was obtained with a scan rate of 2 mVs^{-1} in 1 M Na_2SO_4. In addition, the synthesized material has superior cycling stability. The capacitance retains 97.8% of its initial value after 5000 cycles with a scan rate of 100 mVs^{-1}.

Manuscript submitted May 1, 2014; revised manuscript received June 20, 2014. Published July 3, 2014.

Supercapacitors, also referred to as electrochemical capacitors, have excellent energy storage characteristics, with capacitance values up to 20 to 200 times that of conventional capacitors.[1] They have several other advantages over conventional capacitors, such as higher power density, longer retention time and cycle life, higher discharge efficiency, and stable charge and discharge characteristics.[2] Compared to conventional capacitors, batteries have higher energy density but lower power density. The corresponding values for supercapacitors fall between those for batteries and conventional capacitors.

Supercapacitors can be categorized into three main families, namely electric double-layer capacitors (EDLCs), pseudocapacitors, and hybrid capacitors. EDLCs store electrical energy at the electrode/electrolyte surface. In general, the electrodes used in EDLCs are carbon electrodes, which feature a high specific surface area. Pseudocapacitors store the electrical energy produced by redox reactions (faradaic reactions) on electrodes made of transition metal oxides.[3,4] Hybrid capacitors can be obtained by combining the two aforementioned types.

Among various kinds of metal oxides, manganese dioxide (MnO_2) has been widely used as an electrode material[5–7] due to its excellent chemical properties, low cost, environmental friendliness, and high theoretical capacitance value of 1370 Fg^{-1}.[8] MnO_2 has been commonly used as the active material in energy storage devices such as supercapacitors[8,9] and batteries.[10] However, its compact structure gives it a low specific surface area, and thus low conductivity (10^{-5}∼10^{-6} Scm^{-1})[11] and weak electrolyte permeability.[6,12] MnO_2 is only able to achieve a capacitance value of approximately only 1/5 to 1/6 of its theoretical capacitance.[13] Several polymorphs of MnO_2 are known as α, β, γ, δ, and λ forms. The structures of α, β and γ have 1-D tunnels; the δ form has a 2-D layered structure and the λ form has a 3-D spinel structure.[14] Electrochemical capacitance properties of the polymorphs of MnO_2 were reported[14–16] Layered birnessite MnO_2 is one of the most common structure and a promising electrode material for electrochemical capacitors.[17]

In order to improve the conductivity of MnO_2, considerable research has been done in recent years examining approaches for combining MnO_2 and conductive materials into a composite material. Considering that energy storage in carbon materials is mainly based on the adsorption/desorption mechanism of surface ions and that in manganese dioxide is achieved by redox reactions (faradaic reactions), composites comprising MnO_2 and carbon materials are expected to retain the good properties and performance of the individual materials when used as electrodes in supercapacitors.

Many carbon materials have been studied for use in supercapacitors, including activated carbon, carbon nanocapsules (CNCs), carbon nanotubes (CNTs), graphite, carbon nanofibers (CNFs), and conductive polymers.[18–23] Various methods are available for preparing MnO_2, such as hydrothermal synthesis, co-precipitation, the sol-gel process, the template method, and thermal decomposition.[6,24–29] MnO_2 with various birnessite structures, such as nanobelts,[30,31] flower-like structures,[32] nanobundles,[33] and flower-like nanowhiskers,[34] has been studied. However, the lack of an ideal surface area (usually around 20–150 m^2 g^{-1})[35] reduces the effectiveness of MnO_2 when used as the active material in supercapacitors. Jia et al. thus synthesized a composite comprising MnO_2 and a carbon nanomaterial using the co-precipitation approach, and achieved a capacitance of 186 Fg^{-1} at 2 mVs^{-1}.[36] Zhu et al. evaluated the electrochemical properties of MnO_2 co-assembled on graphene with electrostatic interactions, and obtained a capacitance value of 210 Fg^{-1} with a scan rate of 0.5 Ag^{-1}.[37] In addition, some recent published MnO_2 based core-shell structures for supercapacitors were reported, such as CNT@MnO_2,[38] CNF@MnO_2,[39] PAN@AuPd@MnO_2,[40] and Co_3O_4@MnO_2.[41]

In this study, CNC@MnO_2 core-shell particles with a petal-like morphology were synthesized using a reflux method to coat the surface of CNCs with MnO_2 at a low temperature (90°C). This work investigates the characteristics of the CNC@MnO_2 composite and its synthesis mechanism, and evaluates its electrochemical properties as the active material in supercapacitors.

Experimental

Material preparation.— CNCs with a high specific surface area of 268 (m^2 g^{-1}) were used in this work.[42] The synthesis procedure was as follows. 0.1 g of CNCs was placed into a round flask. 1.58 g of $KMnO_4$ (99% purity) was then added to the flask and dissolved with deionized (DI) water. The $KMnO_4$ solution with CNCs was heated at near 90°C and refluxed for the specified time (10 min to 24 h). The as-produced material in the solution was filtered,rinsed by DI water and then dried in an oven at 100°C overnight.

Characterization.— The crystallinity and bonding energy of the elements of the CNC@MnO_2 particles were analyzed using X-ray diffraction (XRD, Bruker, Smart APEX), X-ray photoelectron spectroscopy (XPS, Kratos, Axis Ultra DLD), and Raman analysis (Horiba, XploRA). The weight percentages of MnO_2 and CNCs were evaluated using thermogravimetric analysis in air (TGA, Perkin-Elmer, Diamond TG/DTA). The morphology and crystal structure of CNC@MnO_2 particles were studied using field-emission scanning electron microscopy (FE-SEM, Hitachi, S-4800) and transmission

*Electrochemical Society Active Member.
[z]E-mail: chmyyl@ccu.edu.tw

electron microscopy (TEM, JEOL, JEM-2010). The surface area was measured using the nitrogen adsorption-desorption method at 77 K (Micrometric, ASPA 2010).

Electrochemical measurements.— For the electrode, CNC@MnO_2 particles were used as the active material (75 wt%), CNCs were used as the conductive material (20 wt%), polyvinylidene difluoride (PVDF) was used as the adhesive (5 wt%), N-methyl-2-pyrrolidone (NMP) was used as the solvent, and graphite (1×1 cm^2) was used as the current collector. The preparation procedure was as follows. PVDF was dissolved in NMP solvent and the resulting PVDF-NMP solution was well mixed with CNC@MnO_2 particles and CNCs. The mixed slurry was then evenly coated onto the surface of graphite. The coated graphite was dried in the oven at 100°C overnight to complete the preparation of the working electrode.

The electrochemical characteristics of the prepared working electrode were analyzed using cyclic voltammetry (CV), the constant-current charge-discharge test, and electrochemical impedance spectroscopy (EIS, Zahner, IM6). The measurements were performed in a three-electrode cell, in which Pt wire and an Ag/AgCl electrode were used as the counter and reference electrodes, respectively. All the electrochemical measurements were conducted at room temperature. An aqueous solution of 1 M Na_2SO_4 was used as the electrolyte. An electrochemical analyzer (CHI, 6081D) was used for CV and galvanostatic charge/discharge measurements, for which the measurement range of the electric potential was set to be 0–1 V, the scan rate was varied from 2–200 mVs^{-1}, and the charge-discharge rate was varied from 0.5–2 Ag^{-1}. EIS was used to obtain the electrochemical impedance spectra, for which the frequency range was varied from 100 mHz to 100 kHz MHz and the alternating-current (AC) voltage amplitude was set to the open-circuit potential of 5 mV.

The specific capacitance can be calculated using:

$$C = \frac{1}{m \times \upsilon \times \Delta V} \int i(V)\, dV \quad [1]$$

$$C = \frac{I \times \Delta t}{m \times \Delta U} \quad [2]$$

where m is the mass of the material, V is the potential scan rate, dV is the potential window in the CV measurement, $i(V)$ is the voltammetric current, I is the supplied current, ΔU is the potential window in the discharge process, and Δt is the discharge time.

Results and Discussion

Structure and morphology.— Figure 1a shows a SEM image of CNCs, which have a uniform particle size of about 20 nm. Figure 1b shows a SEM image of CNC@MnO_2 particles synthesized with a reaction time of 6 h. Their average diameter is 100 nm. As can be seen, the MnO_2 nanostructures nucleated on the surface of the CNCs, forming petal-like particles. This pore structure is beneficial for the mass transport and storage of charges. Figures 1c and 1d show TEM and HR-TEM images of CNC@MnO_2 particles, respectively. As shown, MnO_2 nanoflakes grew on the CNCs, resulting in macro- and mesopore structures. Such structures are beneficial in electrochemical reactions, allowing electrons and ions in the electrolyte to be easily stored in the pores, leading to an improvement in the electrochemical performance.

Figure 2 shows the XRD pattern of CNC@MnO_2 particles. It can be concluded that the composite material is birnessite-type MnO_2 (JCPDS card no. 42–1317)[43] based on the XRD peak values and

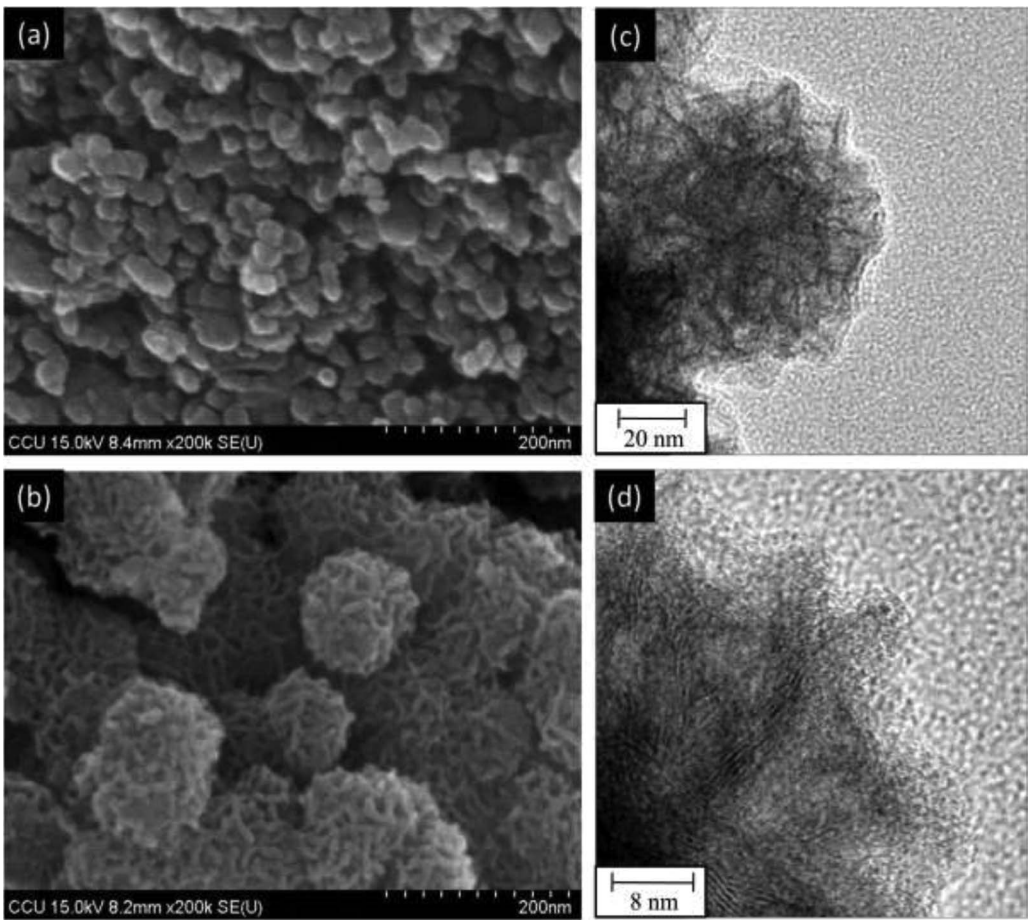

Figure 1. (a) SEM image of CNCs. (b) (c) TEM, and (d) HR-TEM images of CNCs@MnO_2 particles.

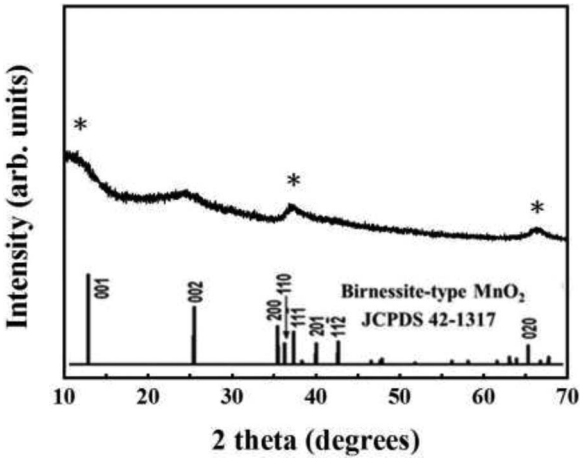

Figure 2. XRD pattern of CNC@MnO_2.

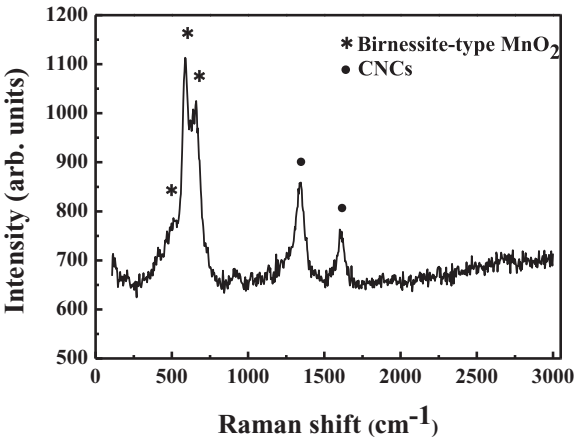

Figure 3. Raman spectrum of CNC@MnO_2 particles.

existing literature. In Figure 2, the three XRD peaks at 12°, 37°, and 66°, respectively, indicate the amorphous phase of birnessite-type MnO_2.[44,45]

Raman spectroscopy was employed to analyze the CNC@MnO_2 particles. Figure 3 shows the obtained Raman spectrum. The peaks at 1350 and 1580 cm^{-1} are attributed to CNCs and the peaks at 575 and 650 cm^{-1} are attributed to MnO_2.[43] The Raman shift at 650 cm^{-1} is due to the symmetric stretching vibration of the Mn-O bond in MnO_6 groups, and that at 575 cm^{-1} is caused by the stretching vibration of the MnO_6 sheet on the substrate. In addition, there is a shoulder peak close to the Raman shift at 575 cm^{-1}, which is usually attributed to the Mn-O stretching vibration in the basal plane of the MnO_6 sheet.[43,46,47]

XPS results for the CNC@MnO_2 particles are given in Figures 4a to 4d. Figure 4a shows the XPS spectrum with a range of 0–900 eV, with peaks corresponding to Mn 3s, C 1s, K 2p, O 1s, and Mn 2p visible. Figure 4b shows the XPS spectrum of Mn 2p. Two peaks corresponding to Mn $2p_{3/2}$ and $2p_{1/2}$ appear at 642.3 and 653.9 eV, respectively, which are attributed to MnO_2.[48] Figure 4c shows the XPS spectrum of Mn 3s, which shows that the energy between the two peaks (ΔE) is about 4.7 eV. Toupin et al.[6] claimed that ΔE values of 5.79, 5.50, 5.41, and 4.78 eV correspond to MnO, Mn_3O_4, Mn_2O_3, and MnO_2, respectively. The as-produced manganese oxide is thus identified as MnO_2. Figure 4d shows the XPS spectrum of O 1s. The peak at 529.9 eV is caused by bonding between Mn and O atoms, which is consistent with the work of Qu et al.[49] Based on these analyzes, it can be concluded that the manganese oxide with a petal-like structure that was coated onto the surface of CNCs was MnO_2. Table I summarizes the XPS results.

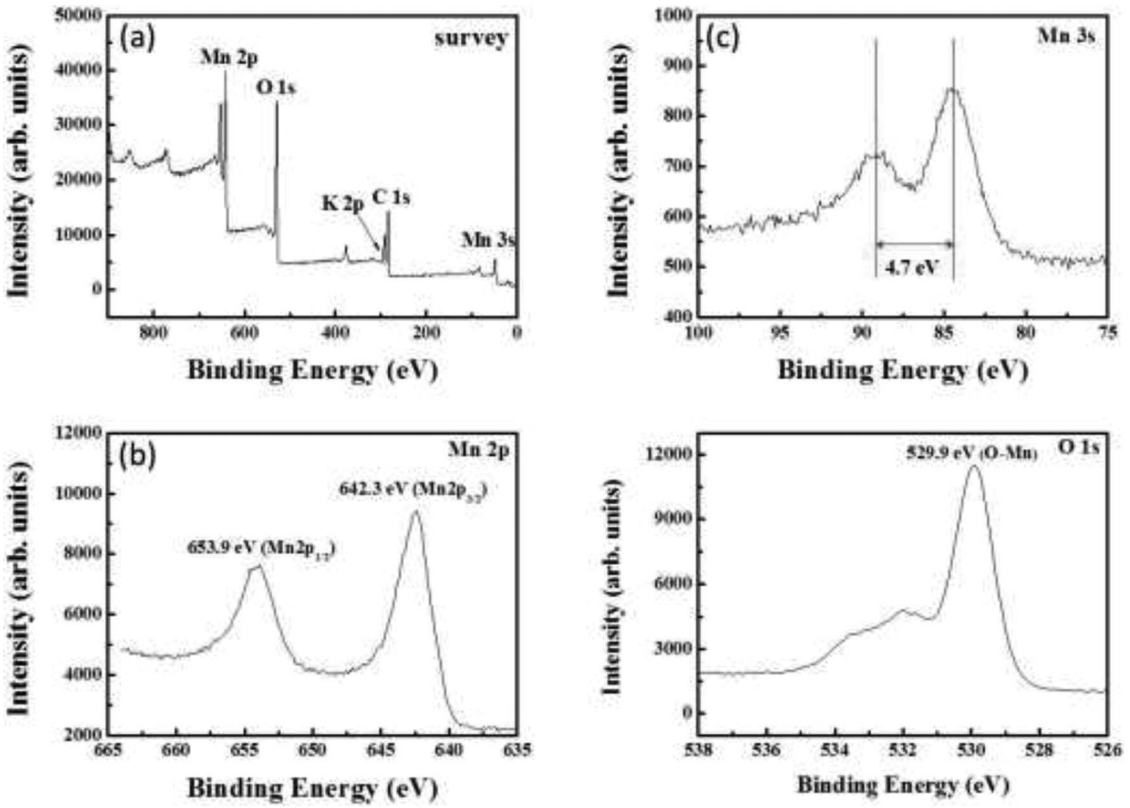

Figure 4. XPS spectra of CNC@MnO_2 particles, (a) Survey, (b) Mn 2p, (c) Mn 3s and (d) O 1s spectra.

Table I. XPS results of CNC@MnO_2 particles.

Mn2p				
Mn2p1/2	Mn2p3/2	Mn3s (ΔE)	O1s	Type
653.9 eV	642.3 eV	4.7 eV	529.9 eV	MnO_2

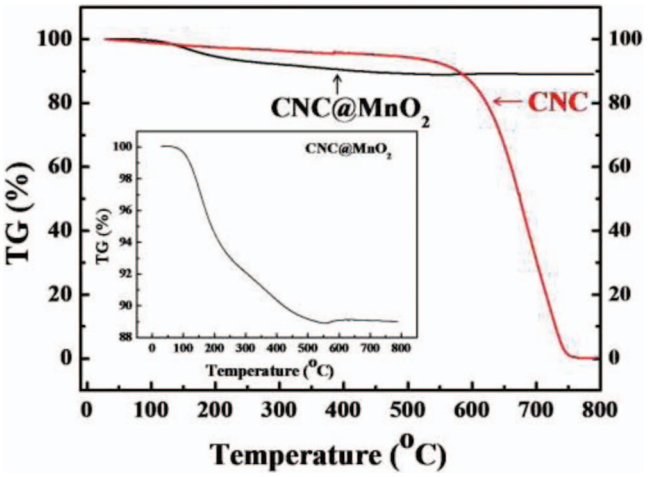

Figure 5. TGA analysis results for CNCs and CNC@MnO_2 particles (inset).

The weight percentages of MnO_2 and CNCs in the composite were obtained using TGA in air. Figure 5 shows the TGA results of CNCs and CNC@MnO_2 particles. For CNCs, the weight decreased slowly before 500°C. It is believed that small amounts of impurities and defects were removed. The weight dropped dramatically above 500°C and the CNCs were burnt completely at 700°C. For CNC@MnO_2 particles (inset of Figure 5), the weight loss before 200°C was likely due to the removal of moisture. The CNC@MnO_2 particles were burnt at 200–500°C. The CNC@MnO_2 particles were oxidized at a lower temperature (200–500°C) compared to that for pure CNCs (500–700°C) because of the catalytic function of MnO_2.[50]

Nitrogen adsorption-desorption isotherms of CNC@MnO_2 particles at 77 K are shown in Figure 6. The isotherms are considered as type IV isotherms with type H3 hysteresis loops, which are the typical isotherms for mesoporous material.[51] The specific surface area is 25.12 m^2 g^{-1}. The pore size distribution of the material calculated using Barret-Joyner-Halenda(BJH) method is given in the inset of Figure 6. The two major pore diameters are 2–2.5 nm and 3.5–4.5 nm. The 2.0–2.5-nm pores are attributed to CNCs and the 3.5–4.5-nm pores are attributed to MnO_2. These results are in good agreement with SEM observations. In general, the size of hydrated ions in the electrolyte is approximately in the range of 0.6–0.73 nm. For maximizing the electrochemical performance of capacitors, the minimum pore diameter should be greater than 0.8 nm for faradaic pseudocapacitance and greater than 1.2 nm for electric double-layer capacitance in order to allow ions to easily transport in and out of the material surface.[52] A diameter of above 5 nm would make hydrated ions easily lose their bonds with the material, decreasing capacitance. Therefore, a pore diameter of 0.8–5 nm is optimal for both pseudocapacitance and electric double-layer capacitance.[53] Table II shows the mesopore (2–20 nm) and micropore (<2 nm) distributions of the CNC@MnO_2 particles obtained from t-plot analysis. The results show that the CNC@MnO_2 particles have suitable pore diameters for both pseudocapacitance and electric double-layer capacitance. However, because of insufficient surface area of the material (25.12 m^2 g^{-1}), we think that the specific capacitance of the CNC@MnO_2 particles is not contributed from electric double-layer capacitance but pseudocapacitance.

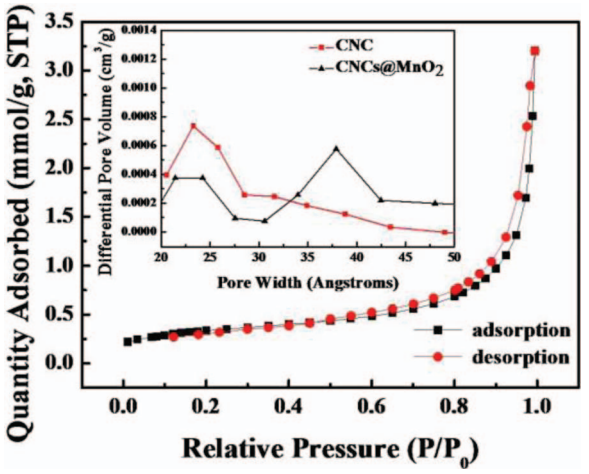

Figure 6. Nitrogen adsorption-desorption isotherms. Inset shows pore diameter distributions.

Growth mechanism.— The morphologies of CNC@MnO_2 particles obtained with various reaction times were studied using SEM. Figures 7a to 7f show the morphologies of CNC@MnO_2 particles synthesized with reaction times of 10 min, 30 min, 1 h, 3 h, 6 h, and 12 h, respectively. As can be seen, petal-like MnO_2 was only obtained after the 1-h reaction. The diameters were from 48 to 87 nm. With increasing reaction time, the petal-like structure became clearer, and the average diameter increased from 87 nm (3 h), to 103 nm (6 h), and to 180 nm (12 h). The proposed growth mechanism of CNC@MnO_2 particles is shown in Figure 8. Nanostructural MnO_2 grown on the surface of carbon materials is based on the redox reaction between carbon and MnO_4^-. The reaction equation can be expressed as:[54]

$$4MnO_4^- + 3C + H_2O \Leftrightarrow 4MnO_2 + CO_3^{2-} + 2HCO_3^- \quad [3]$$

MnO_4^- dissolves in the water solution and reacts with the active sites on the surface of CNCs (defects in the carbon structure), resulting in the nucleation seeds of MnO_2 (see Figure 8c). As the reaction continues, MnO_2 starts to selectively grow from the seed along the preferred crystal orientation, forming MnO_2 nanoflakes, as shown in Figure 8d. As the reaction time continues, all the CNCs become coated with nanoklakes, forming petal-like MnO_2, as shown in Figures 8e and 8f. The diameter of the CNC@MnO_2 particles then increases with increasing reaction time.

Electrochemical properties.— Figure 9a shows the specific capacitance of CNC@MnO_2 particles obtained using CV with a scan range of 0–1 V and a scan rate of 2–200 mVs^{-1}. Samples synthesized with reaction times of 10 min, 30 min, 1 h, 3 h, 6 h, 12 h, and 24 h, respectively, were evaluated. As can be seen, the CNC@MnO_2 particles with a 6-h reaction time had the highest capacitance. The energy storage mechanism can be expressed with the MnO_2 - Na_2SO_4 electrolyte

Table II. Pore characteristics of CNC@MnO_2 particles.

		Pore volume fraction (%)		
BET surface area (m^2 g^{-1})	Average pore diameter (Å)	Micropore	Mesopore	Total pore volume (cm^3 g^{-1})
25.12	173.29	0.016	0.984	0.111

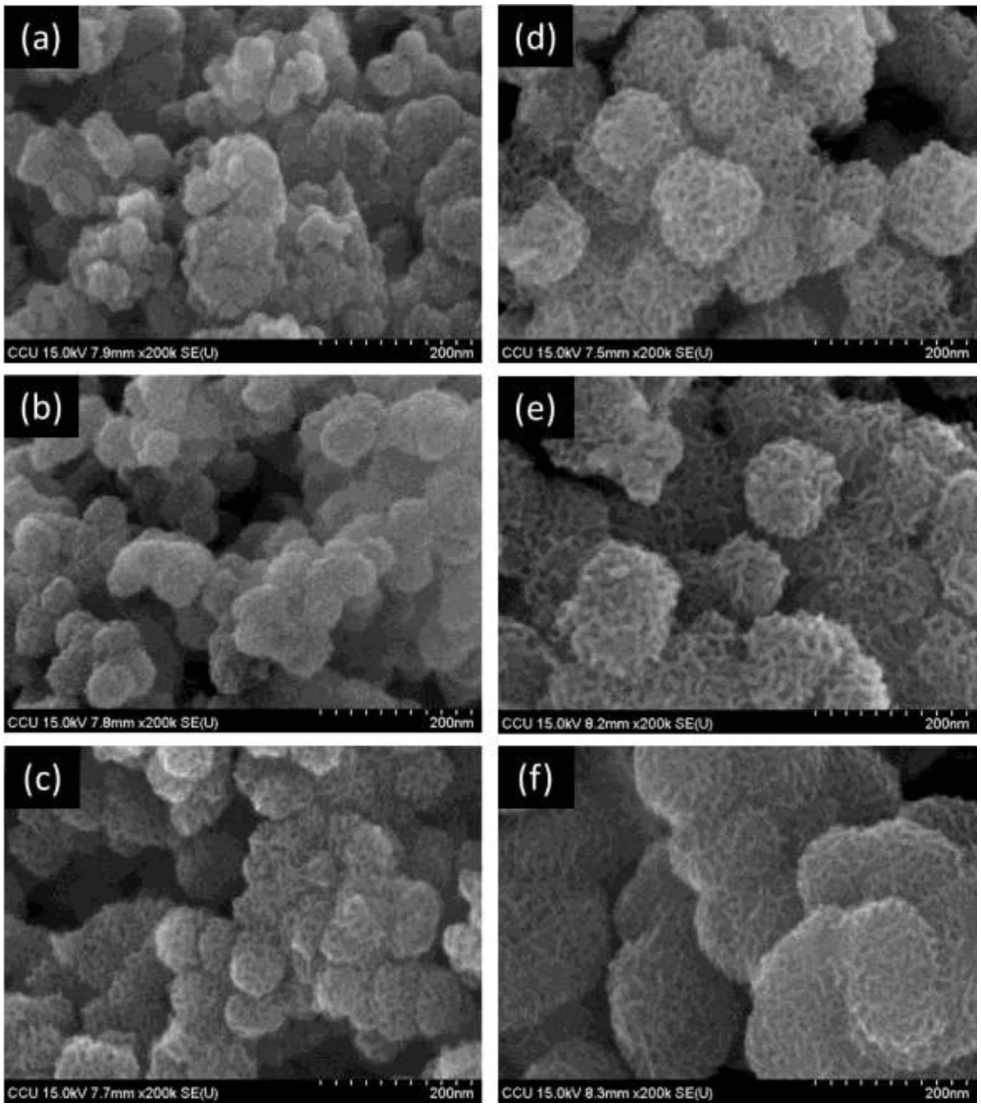

Figure 7. SEM images of CNC@MnO_2 particles synthesized with reaction times of (a) 10 min, (b) 30 min, (c) 1 h, (d) 3 h, (e) 6 h, and (f) 12 h.

system:[35,55]

(1) Surface adsorption/desorption of sodium ions on the MnO_2 electrode, which can be expressed as :

$$(MnO_2)_{surface} + Cation^+ + e^- \leftrightarrow \left(MnO_2^- C^+\right)_{surface} \quad [4]$$

(2) The redox reaction when sodium ions are inserted into and extracted out of the electrode, which can be expressed as:

$$MnO_2 + Cation^+ + e^- \leftrightarrow MnOOC^+ \quad [5]$$

According to the figure, the specific capacitance of CNC@MnO_2 particles increased with increasing reaction time up to 6 h. As the

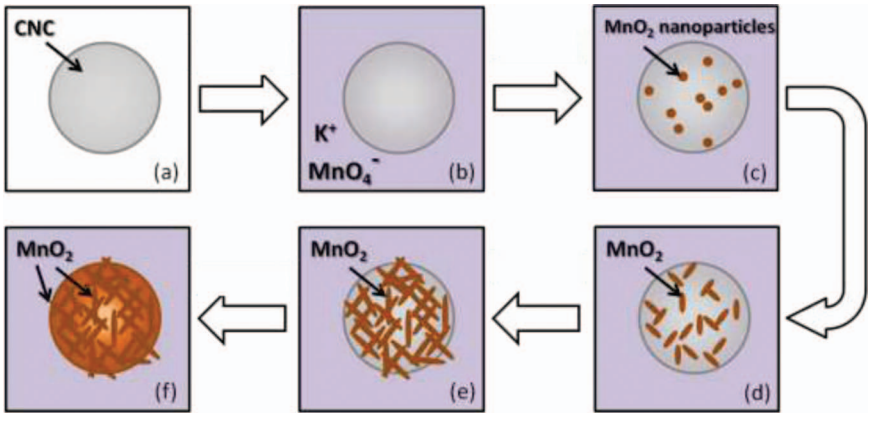

Figure 8. Schematic of proposed growth mechanism of CNC@MnO_2 particles

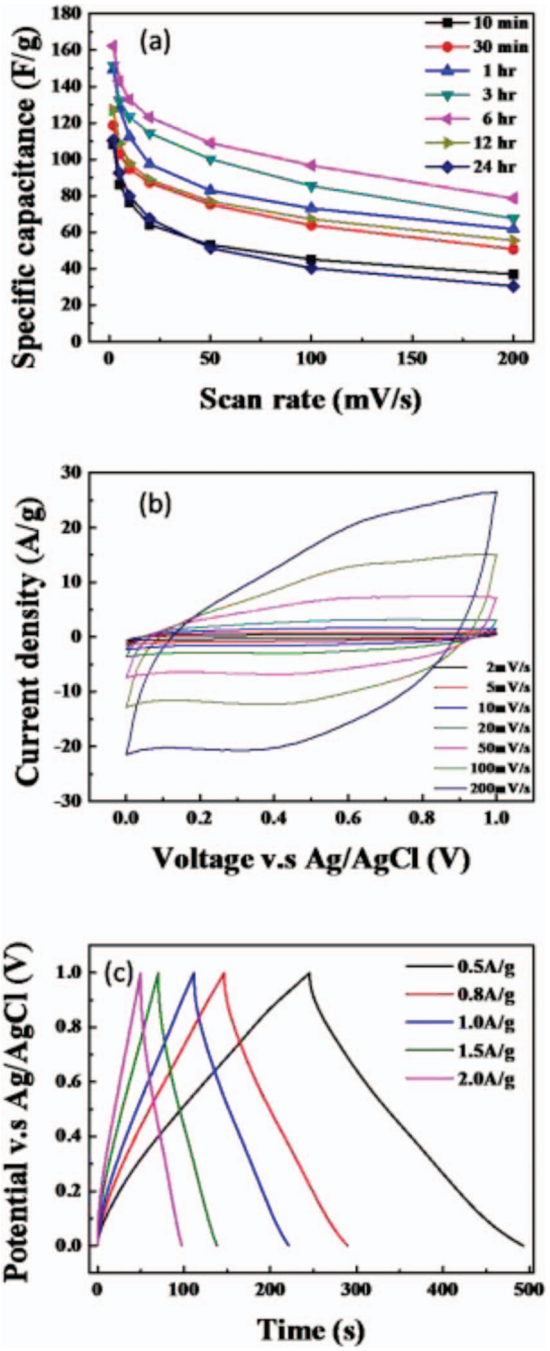

Figure 9. (a) Specific capacitance of CNC@MnO_2 particles synthesized with various reaction times and obtained at various scan rates, (b) CV measurements with various scan rates,and (c) charge-discharge measurements with various current densities.

reaction proceeded, more MnO_2 nanoflake were generated, resulting in an increase in the number of 3–4 nm pores, which are suitable for the insertion and extraction of sodium ions in the MnO_2 electrode. For reflux times beyond 6 h, however, the capacitance starts decreasing due to the increases in the diameter and density of CNC@MnO_2 particles, which hinder the insertion and extraction of sodium ions. Figure 9b shows the CV results of CNC@MnO_2 particles (6-h reaction time) obtained with scan rates of 2, 5, 10, 20, 50, 100, and 200 mVs^{-1}. For all scan rates, the curves show a near symmetric shape. Figure 9c shows galvanostatic charge/discharge measurements of CNC@MnO_2 particles (6-h reaction time) obtained with current densities of 0.5, 0.8, 1, 1.5, and 2 Ag^{-1}. For all current densities, the curves are symmetric triangles. Based on Figures 9b and 9c, the CNC@MnO_2 particles demonstrated good pseudocapacitor performance and high reversibility of the faradaic process.

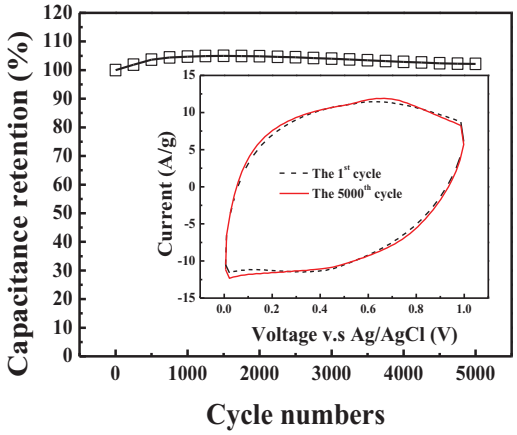

Figure 10. Capacitance retention at 100 mV/s for 5000 cycles and CV measurements with a scan rate of 100 mV/s at 1st and 5000th cycles (inset).

Cycling stability is important for practical supercapacitors. Figure 10 shows the results of 5000 cycles of CV potential sweeps with a scan rate of 100 mVs^{-1}. It can be seen that high cycling stability was achieved, with the capacitance retaining 97.8% of its inital value after 5000 cycles. The inset of the Figure 10 shows the CV curves of the 1st and 5000th cycles. The curve does not change much after 5000 cycles, with the capacitance remaining almost the same as that of the 1st cycle. This cycling stability is higher than previously reported values for MnO_2 composite, such as those for MnO_2/carbon black (91% after 1000 cycles),[36] multi-walled carbon nanotubes/MnO_2 (82.7% after 3500 cycles),[56] MnO_2/graphene (78.7% after 1000 cycles),[57] and graphene-wrapped MnO_2 (82.4% after 1000 cycles).[37] Figures 11a and 11b show SEM images of the electrode morphology before and after 5000 cycles of the CV test, respectively. After 5000 cycles, the morphology of petal-like structure was slightly changed. As is well known, the electric double-layer capacitance is related to the re-arrangement of charges, whereas the pseudocapacitance is related to chemical reactions. Consequently, EDLCs have better electrochemical stability than that of pseudocapacitors, but a lower specific capacitance.[58] In this study, CNCs support the performance associated with electric double-layer capacitance, and MnO_2 nanoflakes support the performance related to specific capacitance. Because MnO_2 was chemically bonded on the surface of the CNCs, the possibility of MnO_2 being dissolved in the electrolyte during CV measurements was reduced. The cycling stability performance was thus improved. It is believed that the specific capacitance of CNC@MnO_2 is mainly contributed from pseudocapacitors due to small surface area of CNC@MnO_2. As a result, the role of CNC in this study is (1) acting as seeds for the growth of CNC@MnO_2 core shell catalyst, and (2) providing electronic path to the MnO_2 for higher rate and (3) more stable cycle performances.

The electrochemical characteristics of the composite were analyzed using EIS in the frequency range of 100 mHz - 100 kHz and a 5-mV AC perturbation at the open-circuit potential. Figure 12 shows the Nyqusit plots before the 1st cycle and after the 5000th cycle. The EIS data was analyzed by fitting it to an equivalent electrical circuit model shown in the inset of the Figure 12. The results obtained from EIS analysis are given in Table III. In the inset of Figure 12, the two impedance spectra are quite similar from the intercept point and the semicircle at high frequency. The intercept with the real axis represents the overall resistance of the electrode material (R_s), including the resistance of the electrode, the resistance of the ions in the electrolyte, and the resistance in between the electrode material and the collector.[59] It was found that after 5000 cycles, R_s slightly decreased from 2.2–1.9 Ω. This might be caused by the increase of pore diameter due to the redox reaction between sodium

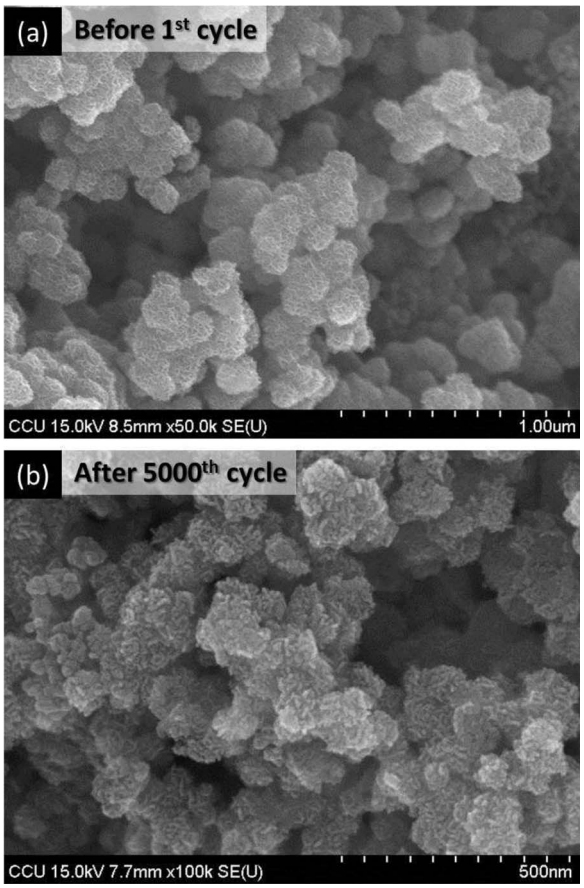

Figure 11. SEM images of CNC@MnO_2 particles (a) before 1st cycle and (b) after 5000th cycle.

ions and MnO_2, making the insertion and extraction of ions easier. In Figure 12, the semicircle, referred to as the Warburg semicircle, is caused by the charge transfer resistance (R_{ct}), which demonstrates the ease of electrochemical reactions between ions in the electrolyte and the interior material of the electrode.[49] After 5000 cycles, R_{ct} increased from 0.22–0.97Ω. The increase in R_{ct} might be associated with the morphological change of the petal-like MnO_2 structure, which increased the resistance of charge transfer. At low frequency, shown

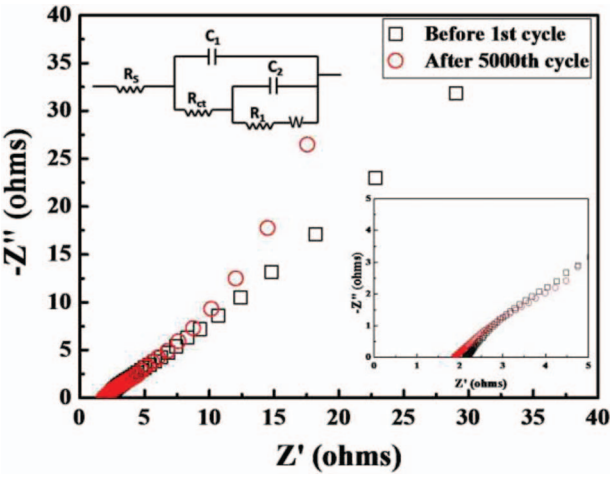

Figure 12. Impedance spectra obtained with a scan rate of 100 mV/s before 1st cycle and after 5000th cycle. Inset shows spectra at low frequency.

Table III. Fitting results of R_s and R_{ct} of CNC@MnO_2 electrodes before 1st cycle and after 5000th cycle.

Resistance	Before 1st cycle	After 5000th cycle
R_s (Ω)	2.2	1.9
R_{ct} (Ω)	0.2261	0.9722

in the inset in the Figure 12 the slope of the inclined line is related to the ease of ion diffusion into the electrode material. The slope increased slightly after 5000 cycles, indicating better mass transport of the ions into the electrode. Based on the impedance studies, it can be concluded that the CNC@MnO_2 particles had high cycling stability and desirable electrochemical characteristics.

Conclusions

In this study, CNC@MnO_2 core-shell particles with a petal-like structure were prepared using a simple approach. Based on XRD, XPS, and Raman analyzes, the obtained petal-like material was confirmed to be birnessite-type MnO_2. A possible growth mechanism of the CNC@MnO_2 material was proposed. The specific capacitance measured by CV with a scan rate of 2 mVs^{-1} was found to be 163 Fg^{-1}. The specific capacitance retained 97.8% of its initial value after 5000 cycles based on cycling stability measurements with a scan rate of 100 mVs^{-1}. The results of the EIS showed that the material performed desirable electrochemical characteristics. Therefore, the CNC@MnO_2 particles have high specific capacitance and excellent cycling stability, making them suitable as the electrode material in supercapacitors.

Acknowledgment

The authors thank the National Science Council of the Republic of China for supporting this research under grant NSC 102–3113-P-194–003.

References

1. R. Kötz and M. Carlen, *Electrochimica Acta.* **45**(15–16), 2483 (2000).
2. J. Jiang and A. Kucernak, *Electrochimica Acta.*, **47**(15), 2381 (2002).
3. L. L. Zhang and X. S. Zhao, *Chemical Society Reviews.* **38**(9), 2520 (2009).
4. Y. P. Zhai, Y. Q. Dou, D. Y. Zhao, P. F. Fulvio, R. T. Mayes, and S. Dai, *Advanced Materials.* **23**(42), 4828 (2011).
5. X. Y. Wang, W. G. Huang, P. J. Sebastian, and S. Gamboa, *Journal of Power Sources.* **140**(1), 211 (2005).
6. M. Toupin, T. Brousse, and D. Belanger, *Chemistry of Materials.* **14**(9), 3946 (2002).
7. L. Athouel, F. Moser, R. Dugas, O. Crosnier, D. Belanger, and T. Brousse, *Journal of Physical Chemistry C.* **112**(18), 7270 (2008).
8. L. G. Xue, H. Hao, Z. Wei, T. Huang, and A. S. Yu, *Journal of Solid State Electrochemistry.* **15**(3), 485 (2011).
9. C. J. Xu, C. G. Wei, B. H. Li, F. Y. Kang, and Z. C. Guan, *Journal of Power Sources.* **196**(18), 7854 (2011).
10. F. Jiao and P. G. Bruce, *Advanced Materials.* **19**(5), 657 (2007).
11. L. Li, Z. Y. Qin, L. F. Wang, H. J. Liu, and M. F. Zhu, *Journal of Nanoparticle Research.* **12**(7), 2349 (2010).
12. S. Devaraj and N. Munichandraiah, *Electrochemical and Solid State Letters.* **8**(7), A373 (2005).
13. C. Y. Wan, K. Azumi, and H. Konno, *Electrochimica Acta.* **52**(9), 3061 (2007).
14. S. Devaraj and N. Munichandraiah, *Journal of Physical Chemistry C.* **112**(11), 4406 (2008).
15. T. Brousse, M. Toupin, R. Dugas, L. Athouel, O. Crosnier, and D. Belanger, *Journal of the Electrochemical Society.* **153**(12), A2171 (2006).
16. C. H. Wang, H. C. Hsu, and J. H. Hu, *Journal of Power Sources.* **249**, 1 (2014).
17. D. P. Dubal, D. S. Dhawale, R. R. Salunkhe, and C. D. Lokhande, *Journal of Electroanalytical Chemistry.* **647**(1), 60 (2010).
18. Z. P. Li, J. Q. Wang, S. Liu, X. H. Liu, and S. R. Yang, *Journal of Power Sources.* **196**(19), 8160 (2011).
19. J. H. Kim, K. H. Lee, L. J. Overzet, and G. S. Lee, *Nano Letters.* **11**(7), 2611 (2011).
20. J. Yan, Z. J. Fan, T. Wei, W. Z. Qian, M. L. Zhang, and F. Wei, *Carbon.* **48**(13), 3825 (2010).
21. R. Liu, J. Duay, and S. B. Lee, *Acs Nano.* **5**(7), 5608 (2011).
22. L. H. Bao, J. F. Zang, and X. D. Li, *Nano Letters.* **11**(3), 1215 (2011).
23. C. W. Huang, Y. T. Wu, C. C. Hu, and Y. Y. Li, *Journal of Power Sources.* **172**(1), 460 (2007).
24. H. Kim and B. N. Popov, *Journal of the Electrochemical Society.* **150**(3), D56 (2003).

25. Y. U. Jeong and A. Manthiram, *Journal of the Electrochemical Society.* **149**(11), A1419 (2002).
26. H. Y. Lee and J. B. Goodenough, *Journal of Solid State Chemistry.* **144**(1), 220 (1999).
27. M. Toupin, T. Brousse, and D. Belanger, *Chemistry of Materials.* **16**(16), 3184 (2004).
28. R. N. Reddy and R. G. Reddy, *Journal of Power Sources.* **124**(1), 330 (2003).
29. R. N. Reddy and R. G. Reddy, *Journal of Power Sources.* **132**(1–2), 315 (2004).
30. R. H. Ma, Y. Bando, L. Q. Zhang, and T. Sasaki, *Advanced Materials.* **16**(11), 918 (2004).
31. Z. Liu, R. Ma, Y. Ebina, K. Takada, and T. Sasaki, *Chemistry of Materials.* **19**(26), 6504 (2007).
32. L. C. Zhang, L. P. Kang, H. Lv, Z. K. Su, K. Ooi, and Z. H. Liu, *Journal of Materials Research.* **23**(3), 780 (2008).
33. J. C. Ge, L. H. Zhuo, F. Yang, B. Tang, L. Z. Wu, and C. H. Tung, *Journal of Physical Chemistry B.* **110**(36), 17854 (2006).
34. V. Subramanian, H. W. Zhu, and B. Q. Wei, *Journal of Power Sources.* **159**(1), 361 (2006).
35. V. Subramanian, H. W. Zhu, R. Vajtai, P. M. Ajayan, and B. Q. Wei, *Journal of Physical Chemistry B.* **109**(43), 20207 (2005).
36. F. Jia, M. M. Chen, C. Y. Wang, J. Wang, and J. M. Zheng, *Materials Letters.* **78**, 127 (2012).
37. J. Y. Zhu and J. H. He, *Acs Applied Materials and Interfaces.* **4**(3), 1770 (2012).
38. A. L. M. Reddy, M. M. Shaijumon, S. R. Gowda, and P. M. Ajayan, *Journal of Physical Chemistry C.* **114**(1), 658 (2010).
39. O. Ghodbane, M. Louro, L. Coustan, A. Patru, and F. Favier, *Journal of the Electrochemical Society.* **160**(11), A2315 (2013).
40. Z. N. Yu, B. Duong, D. Abbitt, and J. Thomas, *Advanced Materials.* **25**(24), 3302 (2013).
41. J. P. Liu, J. Jiang, C. W. Cheng, H. X. Li, J. X. Zhang, and H. Gong, et al *Advanced Materials.* **23**(18), 2076 (2011).
42. T. C. Liu and Y. Y. Li, *Carbon.* **44**(10), 2045 (2006).
43. S. B. Ma, Y. H. Lee, K. Y. Ahn, C. M. Kim, K. H. Oh, and K. B. Kim, *Journal of the Electrochemical Society.* **153**(1), C27 (2006).
44. S. B. Ma, K. Y. Ahn, E. S. Lee, K. H. Oh, and K. B. Kim, *Carbon.* **45**(2), 375 (2007).
45. W. F. Wei, X. W. Cui, W. X. Chen, and D. G. Ivey, *Chemical Society Reviews.* **40**(3), 1697 (2011).
46. C. Julien, M. Massot, R. Baddour-Hadjean, S. Franger, S. Bach, and J. P. Pereira-Ramos, *Solid State Ionics.* **159**(3–4), 345 (2003).
47. C. M. Julien, M. Massot, and C. Poinsignon, *Spectrochimica Acta Part a-Molecular and Biomolecular Spectroscopy.* **60**(3), 689 (2004).
48. B. X. Li, G. X. Rong, Y. Xie, L. F. Huang, and C. Q. Feng, *Inorganic Chemistry.* **45**(16), 6404 (2006).
49. Q. T. Qu, P. Zhang, B. Wang, Y. H. Chen, S. Tian, and Y. P. Wu, et al *Journal of Physical Chemistry C.* **113**(31), 14020 (2009).
50. L. L. Zhang, T. X. Wei, W. J. Wang, and X. S. Zhao, *Microporous and Mesoporous Materials.* **123**(1–3), 260 (2009).
51. G. Leofanti, M. Padovan, G. Tozzola, and B. Venturelli, *Catalysis Today.* **41**(1–3), 207 (1998).
52. L. Cao, M. Lu, and H. L. Li, *Journal of the Electrochemical Society.* **152**(5), A871 (2005).
53. K. H. An, W. S. Kim, Y. S. Park, Y. C. Choi, S. M. Lee, and D. C. Chung, et al *Advanced Materials.* **13**(7), 497 (2001).
54. X. Jin, W. Zhou, S. Zhang, and G. Z. Chen, *Small.* **3**(9), 1513 (2007).
55. S. C. Pang, M. A. Anderson, and T. W. Chapman, *Journal of the Electrochemical Society.* **147**(2), 444 (2000).
56. H. J. Zheng, J. X. Wang, Y. Jia, and C. A. Ma, *Journal of Power Sources.* **216**, 508 (2012).
57. Y. Li, N. Q. Zhao, C. S. Shi, E. Z. Liu, and C. N. He, *Journal of Physical Chemistry C.* **116**(48), 25226 (2012).
58. M. Winter and R. J. Brodd, *Chemical Reviews.* **104**(10), 4245 (2004).
59. J. Gamby, P. L. Taberna, P. Simon, J. F. Fauvarque, and M. Chesneau, *Journal of Power Sources.* **101**(1), 109 (2001).